Bridging nanoindentation and triaxial creep tests on a shale

Yingxiao Liu[1] · Alexandra C. Burch[2] · Kane C. Bennett[2] · Younane Abousleiman[3] · Ronaldo I. Borja[1,*]

[1] Department of Civil and Environmental Engineering, Stanford University, Stanford, California 94305, USA
[2] Los Alamos National Laboratory, Los Alamos, New Mexico 87545, USA
[3] PoroMechanics Institute, University of Oklahoma, Norman, Oklahoma 73019, USA
[*] borja@stanford.edu

Summary. Shale is known to exhibit significant creep across spatiotemporal scales. In this work, we performed indentation and triaxial creep tests on organic-rich Woodford shale and showed that the measured creep responses at the nanometer and millimeter scales are statistically correlated in the sense that the indentation creep tests can be used to predict the triaxial creep response. The link between the two extreme scales is facilitated by an elasto-viscoplastic constitutive model based on critical state theory. Even though this constitutive model contains several material parameters, only the elastic modulus and viscosity played a major role in statistically correlating the creep responses at the two scales. Given that shale is commonly represented as a transversely isotropic material, we conducted indentation and triaxial creep tests in both bed-normal (BN) and bed-parallel (BP) directions on the rock samples. For the shale that was tested, the creep responses at the nanometer and millimeter scales were statistically correlated in the BN direction where the rock is weaker. However, the creep deformations at the two scales in the BP direction, where the rock is stronger, were significantly smaller than in the BN direction, and so, they were not as strongly correlated. Nevertheless, the results of this study suggest that shale exhibits strongly anisotropic creep properties.

Keywords. creep, nanoindentation, shale, triaxial test

1 Introduction

Shale is the most common sedimentary rock found on or near the surface of Earth [10, 61]. Its high organic content and low permeability are ideal for hydrocarbon exploration and storage [18, 74, 82], carbon sequestration [53, 54], and for use as a seal in nuclear waste repository [76]. Shale is also one of the most complex materials to model due to its heterogeneous microstructure. In

particular, shale exhibits pronounced viscous creep behavior that manifests in the laboratory and in the field [2, 19, 34, 39]. This time-dependent behavior may be related to the growth of subcritical cracks [16, 17, 21, 30, 41], intragranular and/or intergranular slipping [8, 25], rearrangement of clay particles under external loads [31, 79], compaction of the pore spaces [72], and/or poromechanical effects [13, 15, 23, 32, 33, 52]. The long-term creep deformation in a shale deposit is crucial for land subsidence prediction [19, 49] and borehole stability assessment [34, 38, 44, 58]. However, prediction of the creep deformation remains a challenging problem for modelers because shale exhibits multiscale heterogeneity and anisotropy due to its complex mineral composition and history of formation [1, 11, 22, 35–37, 57, 59, 66–68, 83, 86].

The creep behavior of shale is traditionally investigated in the laboratory with triaxial creep tests, where it has been reported in the literature that creep deformations can be triggered even at low stress levels [6, 45, 56, 62, 63, 72, 73]. It has also been observed that the steady-state creep strain rate increases almost linearly with differential stress, and is not significantly affected by the confining pressure [40, 45, 73]. Most experiments have shown that shale samples develop much larger axial creep strains when loaded in the bed-normal (BN) direction than when loaded in the bed-parallel (BP) direction. In either case, the measured lateral creep strains are usually much smaller than the measured axial creep strains [63, 72, 73]. Several empirical creep laws have been developed from triaxial creep tests on shale, including the power creep law [20, 26, 48, 80] and the logarithmic creep law [19, 50, 55, 64]. They are generally accurate for time periods ranging from hours to days, but the applicability of triaxial creep tests in practice is limited by the size of the samples and duration of the tests. Intact shale samples with sizes on the order of inches are required for the tests, which are generally not available because of the limitations in the field sampling procedure [48, 69]. Furthermore, triaxial creep tests are very time-consuming to conduct, usually lasting days if not weeks to complete [24, 51, 63, 72].

Recently, indentation tests have been used to investigate the creep behavior of shale [5, 9, 27, 29, 42, 43, 46, 69, 77]. An advantage of these tests is that they only last a few minutes, enabling the generation of multiple indentation response curves spatially in a grid pattern [47, 55]. The anisotropy of a sample can also be investigated by indenting in different directions relative to the bedding plane [7]. However, because of the material's complex mineral composition and the very small size of the sample being tested, the results could exhibit significant spatial variability especially when different minerals of the rock are indented. To obtain a more meaningful interpretation of results, indentation curves for the soft phase (clay and organic matters) can be separated from the curves for the hard phase (quartz, feldspar and pyrite), as done by a few authors [7, 55], but even then, indentation curves on the same phase can exhibit significant variability. In addition, most authors only use the indentation curves to infer the elastic modulus and hardness of the rock

[78], even though the response of the rock during indentation is not purely elastic.

To sum up, creep data from indentation tests can be generated more easily, but they are subject to significant variability due to the material's complex composition and heterogeneous microstructure. On the other hand, triaxial creep tests require larger samples and take longer to conduct, and therefore, fewer response data can be obtained even with large samples. Yin et al. [81] attempted to bridge the creep behaviors across the two scales with a recently developed Cam-Clay IX model [11] by treating shale as a mixture of a soft phase and a hard phase. They calibrated the material parameters of the soft phase with nanoindentation data, back-calculated the properties of the hard phase with microindentation data, and upscaled the creep response of the shale to the triaxial scale. However, their work was incomplete because of the lack of experimental data to fully validate their model at the triaxial scale.

In this paper, we adopt a statistical approach to upscaling the creep behavior of an organic-rich Woodford shale [3, 4] aimed at correlating the indentation test data with triaxial creep data. We validate the approach by conducting indentation and triaxial creep tests on the same shale samples in both BN and BP directions. We utilize the Cam-Clay IX model to facilitate the interpretation of results at the two scales of the tests. In addition, we quantify the mineral composition of the shale with X-ray photoelectron spectroscopy (XPS) and X-ray diffraction (XRD) to characterize the microstructural composition of the shale samples. Results of the analysis suggest a strongly anisotropic behavior of the shale in both the (rate-independent) elastoplastic and (rate-dependent) creep responses. We show that the indentation and triaxial creep data are strongly correlated in the weaker BN direction, but the correlation is not as strong in the stronger BP direction because the measured creep deformations in that direction are very small in comparison to the measured creep deformations in the BN direction.

2 Theory

This section gives an overview of how nanoindentation creep tests can be used to predict the results of triaxial creep tests. The bridge between the two tests is facilitated by Cam-Clay IX, a transversely isotropic, viscoplastic constitutive model based on critical state theory developed by the Stanford group [11]. Because the two tests are orders of magnitude apart on the metric scale, statistical analysis is necessary to link the two scales. We first give an overview of the scale-bridging technique, after which, we describe the important features of the viscoplastic model. Fluid flow is not considered in the present work, see [12, 86–88].

2.1 Overview of the methodology

In indentation tests the load on the indenter is applied at a certain rate, is held fixed for around 60 seconds at the peak value, and then is gradually removed. During the stage of experiment when the load is held fixed, the indenter accumulates a certain amount of penetration into the shale that is used to estimate the creep properties of the rock. Viscoplastic constitutive models formulated based on the concept of overstress rely mainly on the elastic moduli and viscosities for predicting the creep response, and this is also true with the constitutive model used in this study. A major challenge with interpreting the results of indentation experiments on shale is that the measured creep behavior can vary significantly from point to point within a small sample due to the inherent heterogeneity of the rock. However, for the shale tested in this work, we observed that during the steady creep stage of the experiment the indentation-time curves are nearly parallel to each other in the BN and BP directions. This allows the calibration of the elastic moduli and viscosities of the rock in these two directions.

Indentation creep tests produce a large number of indentation-time curves each one of which can be used to back-figure the corresponding local elastic modulus and viscosity at the indented point. These two materials parameters are back-figured by conducting a finite element (FE) simulation of the indentation creep test using the Cam-Clay IX viscoplastic constitutive model. In principle, one can always simulate each indentation, but this would be very expensive and time-consuming to conduct given the large number of indented points. Instead, we only simulate a few indentations and use linear interpolation to determine the material parameters for the test results that lie in between the tests that have been simulated. We then generate a bar chart or histogram representing the number of occurrences of a range of values of the elastic moduli and viscosities, and the median values are used to simulate the triaxial creep tests. Because indentation data for the shale are available for loading in both BN and BP directions, we can constrain the required material parameters for simulating the triaxial creep tests.

2.2 Viscoplastic model

The viscoplastic framework adopted in this study is based on the so-called overstress model. In this model, the stress point can live in stress space outside the yield surface, but gets attracted to the yield surface. Denoting the yield function as f, the stress point in the inelastic regime lives in the space where $f > 0$ but gets attracted to the locus of points where $f = 0$. The kinematics of the theory calls for the stress point $\boldsymbol{\sigma}$ to move back to the yield surface, where $f = 0$, at a rate that is proportional to its distance from the yield surface and inversely proportional to the viscosity of the material. In creep, however, the stress point $\boldsymbol{\sigma}$ is fixed and it is the yield surface $f = 0$ that is allowed to expand to catch this stress point.

The total strain rate tensor $\dot{\boldsymbol{\epsilon}}$ is assumed to be decomposed additively into an elastic part $\dot{\boldsymbol{\epsilon}}^e$ and a viscoplastic part $\dot{\boldsymbol{\epsilon}}^{vp}$, i.e.,

$$\dot{\boldsymbol{\epsilon}} = \dot{\boldsymbol{\epsilon}}^e + \dot{\boldsymbol{\epsilon}}^{vp} \,. \tag{1}$$

The viscoplastic strain rate tensor has a form analogous to the flow rule used in rate-independent elastoplasticity [14]. There are two commonly used forms for $\dot{\boldsymbol{\epsilon}}^{vp}$, namely, the form proposed by Perzyna [60],

$$\dot{\boldsymbol{\epsilon}}^{vp} = \frac{\langle f \rangle}{\eta} \frac{\partial f}{\partial \boldsymbol{\sigma}} \,, \tag{2}$$

and the form proposed by Duvaut and Lions [28],

$$\dot{\boldsymbol{\epsilon}}^{vp} = \frac{1}{\tau} \boldsymbol{c}^{e-1} : (\boldsymbol{\sigma} - \boldsymbol{\sigma}^{\circ}) \,, \tag{3}$$

where $\boldsymbol{c}^e$ is the elasticity tensor for the material, $\boldsymbol{\sigma}^{\circ}$ is 'closest point' associated with the rate-independent state, and the symbols $\langle \cdot \rangle$ are the Macauley brackets. Each form contains a parameter that may be correlated with the creep properties of the material. In the Perzyna model, the parameter is the viscosity coefficient η, whereas in the Duvaut-Lions model, it is the relaxation time τ.

The rate-constitutive equation for the Perzyna model takes the form

$$\dot{\boldsymbol{\sigma}} = \boldsymbol{c}^e : \dot{\boldsymbol{\epsilon}} - \langle f \rangle \frac{\boldsymbol{c}^e}{\eta} : \frac{\partial f}{\partial \boldsymbol{\sigma}} \,. \tag{4}$$

The first term on the right-hand side of this equation is the elastic stress predictor, whereas the second term is the rate-dependent stress relaxation, which depends mainly on the elastic stiffness and viscosity. Similarly, for the Duvaut-Lions model the rate-constitutive equation takes the form

$$\dot{\boldsymbol{\sigma}} = \boldsymbol{c}^e : \dot{\boldsymbol{\epsilon}} - \frac{1}{\tau} (\boldsymbol{\sigma} - \boldsymbol{\sigma}^{\circ}) \,, \tag{5}$$

where we see that the model parameter for the stress relaxation term is the relaxation time τ. This material parameter depends on the viscosity and stiffness of the material. For example, in 1D theory the relaxation time $\tau = \eta / E$, where E is the Young's modulus of elasticity [70]. Whatever the model, we see that the two dominant material parameters during creep deformation are the elastic moduli and viscosities of the material.

The Cam-Clay IX model adopts the overstress viscoplastic theory employing both the Perzyna and Duvaut-Lions formulations [11]. Experience with these two formulations suggest that there is not much difference in the predicted creep deformations between the two models [11], and that it is just a matter of preference whether one chooses one formulation or the other. In this work, we choose the Perzyna formulation. The Cam-Clay IX model

groups the shale components into a stiff part (quartz, feldspar, pyrite, and carbonates) and a soft part (clay and kerogen), where each part is modeled as an elasto-viscoplastic material with a rotated ellipsoidal yield surface appropriate for a transversely isotropic material [65, 85, 89]. However, because we aim to average the material properties for upscaling to the triaxial scale, we simply assume in this work that each indented point can be represented by a single set of material constants (i.e., Young's modulus and viscosity) that can be back-figured from the indentation-time curve developed for the indented point. Figure 1 shows a plot of the yield surface on the p-q plane (first and second invariants of the stress tensor, respectively) with the stress point $\boldsymbol{\sigma}$ living in the region where $f > 0$ and $\boldsymbol{\sigma}^\circ$ is its 'closest point.' We note that in the elastic range the rock is also modeled as a transversely isotropic material with five elastic constants that include the elastic Young's moduli in the BN and BP directions [65].

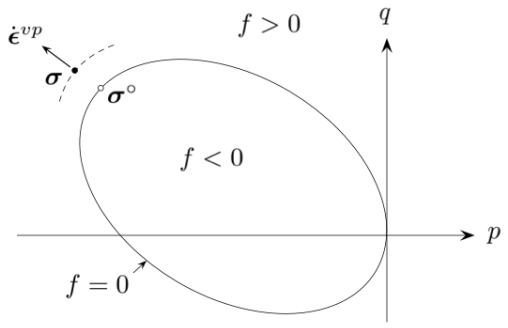

Fig. 1: Overstress viscoplastic framework employing a rotated ellipsoidal yield surface of modified Cam-Clay model. During creep, the stress point $\boldsymbol{\sigma}$ is fixed while the yield surface $f = 0$ expands toward the stress point.

3 Experiments

This section describes the following laboratory tests performed on the Woodford shale sample: (a) material characterization, (b) nanoindentation tests, and (c) triaxial creep tests.

3.1 Material characterization

The mineralogica and chemical information of the shale sample was obtained from X-ray photoelectron spectroscopy (XPS) and X-ray diffraction (XRD)

tests. For XPS tests conducted under a high vacuum condition, different atoms in the sample were identified based on the binding energy of the photoelectrons to their original orbitals, while for XRD tests unique crystalline cell structures were used to characterize different minerals.

The XPS test was conducted at the Stanford Nano Shared Facilities (SNSF) with the PHI VersaProbe III microprobe. The shale sample was crushed into powder, stuck to the substrate with a double-sided carbon tap, transferred to the intro chamber and vacuumed by a turbo pump until the pressure dropped below 10^{-4} Pa. The sample was then moved into the main chamber where the system was further vacuumed to a pressure of 10^{-6} Pa. An X-ray source with the output of 50 W and voltage of 15 kV was used to survey the sample over a binding energy range from 0 to 1200 eV with a step size of 0.8 eV. The spectrum of the shale powder is shown in Figure 2.

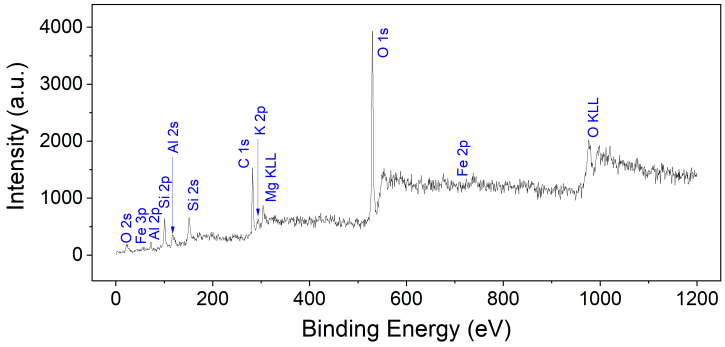

Fig. 2: XPS spectrum of shale sample.

The vertical axis of the spectrum presents the signal intensity and is in unit of counts per second (CSP), but since only the relative intensity of different signals matters, it is common practice to use arbitrary unit (a.u.) to denote the signal intensity. From the primary photoelectron signals, which are shown as the sharp tall peaks in the spectrum, we can identify the O, Mg, Al, Si and Fe elements in the sample. The area of the peaks were then used to calculate the atomic ratio, and the result is listed in Table 1.

We see that the dominant elements in our sample are O, C and Si, and the ratio between O and Si is very close to 1:2. Element K and Al are present in the clay (e.g. illite), while element C is present in the oil and kerogen. No Ca was identified from the sample, indicating that calcite is not a main component of the sample. The weight ratio between quartz and clay was approximately 2:1.

The XRD test was performed using the Rigaku MiniFlex 600 diffractometer. A small amount of shale powder was dumped on the mirror surface of the zero background holder and distributed evenly via circular motions. The

Element	Orbital	Peak Center (eV)	Peak Area	RSF	Atomic Ratio (%)
O	1s	530	12868.6	2.93	41.07
C	1s	282.5	3224.5	1	30.15
Si	2p	100.7	1723.9	0.817	19.73
Al	2p	72.6	411	0.537	7.16
K	2p	294.1	683	3.97	1.61
Fe	2p	708.8	487	16.42	0.28

Table 1: Elements identified from the XPS spectrum. RSF = Relative Sensitivity Factor.

holder was then inserted into the auto sampler inside the chamber and the beam knife was set down to prevent the X-ray from scattering. The measurement was taken at a voltage of 40 kV and a current of 15 mA. The scanning range 2θ was set from 10 to 90° with a step size of 0.02° and a scanning speed of 5°/min. The resulting XRD pattern is shown in Figure 3.

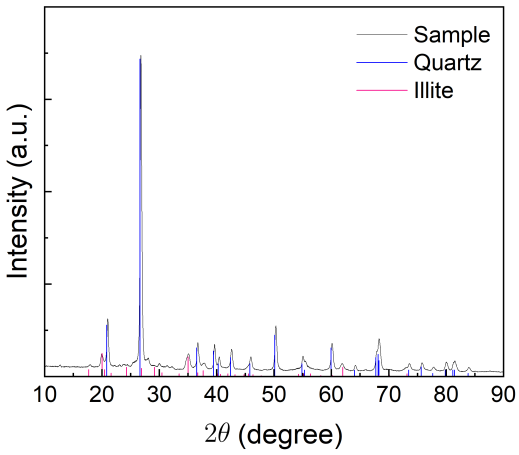

Fig. 3: Match of XRD patterns for quartz, illite, and the shale sample.

Mineral identification was performed by individually matching each peak in the XRD pattern with those of different minerals. The common minerals contained in shale, with an available powder diffraction file (PDF) in the PDF-4 database, are quartz (SiO_2), calcite ($CaCO_3$), pyrite (FeS_2), illite ($KAl_2(Si,Al)_4O_{10}(OH)_2$) and kaolinite ($Al_2Si_2O_5(OH)_4$). Among these minerals, only quartz and illite were confirmed to be present, as shown in Figure 3. By using the reference intensity ratio (RIR) method and selecting the

highest peak centered at 26.6° for quartz, and the symmetric peak centered at 62.0° for illite, the weight ratio of the two minerals was estimated as 1.86:1. This ratio agrees well with the number calculated from the XPS test.

3.2 Nanoindentation tests

Nanoindentation tests on a small piece of shale sample were conducted on a Hysitron TI-950 Triboindenter with a maximum load of 13 mN at the Los Alamos National Laboratory. The sample was first polished before being mounted on the instrument, with the surface roughness measured using scanning probe microscopy (SPM) to range from 5 to 15 nm. All indents were performed using a diamond Berkovich indenter probe with a half angle of 65.27°. The load on the indenter was increased from zero to approximately 491 μN over a period of 30 s, and was held constant at the peak value for 60 s. Such a short hold period can provide more consistent results and more data points for statistical analysis. During the whole process, the vertical displacement of the indenter was continuously recorded. In total, 63 indentation creep curves along the BN direction and 86 curves along the BP direction were recorded. Results from the tests are shown in Figures 4 and 5.

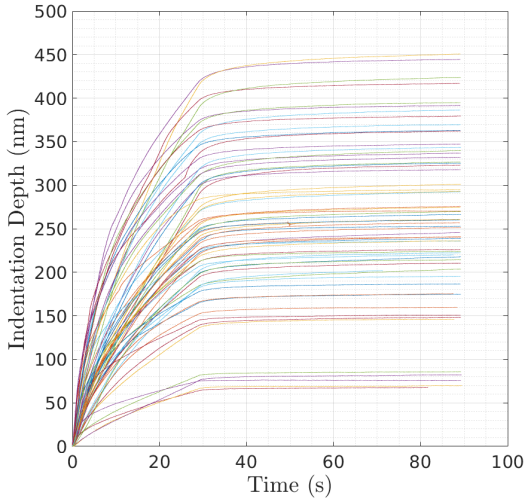

Fig. 4: Vertical displacement versus time along the BN direction.

A first observation is that the indentation depth-time curves were scattered over a wide range, indicating that the elasto-viscoplastic responses of the material varied significantly from point to point within the sample. This affirms that the nanoindentation tests can quantify the mineral-level heterogeneity of the shale sample. Under the same load, the maximum indentation

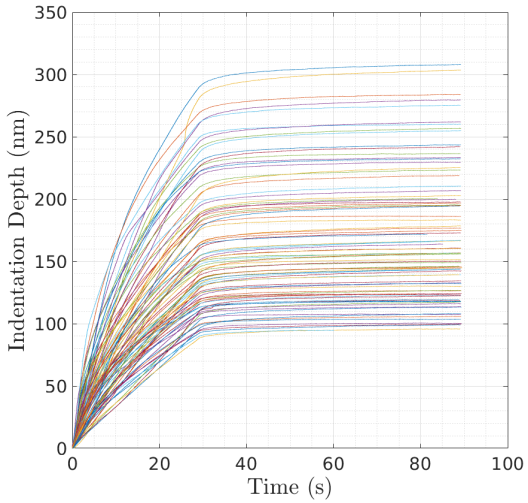

Fig. 5: Vertical displacement versus time along the BP direction.

depth varied from about 70 nm to 450 nm along the BN direction, and from 100 nm to 310 nm along the BP direction. This variation is due to the heterogeneity of the shale at the nanometer scale: hard crystalline minerals such as quartz, feldspar, and pyrite behaved much harder when they were indented as compared to the responses of clay or organic matter when subjected to the same load. In fact, four indentation curves at the bottom of Figure 4 appeared to fall on locally hard minerals and were identified as outliers in that they were separated from the rest of the indentation curves by a significant spacing.

Focusing on the evolution of indentation depth with time during the creep stage, we see two different phases for each curve: an initial creep phase where the creep rate decreases with time, and a steady creep phase where the creep rate is constant and the penetration of the indenter increases linearly with time. We also observe that minerals with different elasto-plastic properties manifest these properties during the initial creep phase, but when they enter the steady creep stage, all curves become nearly straight. This feature is observed in both BN and BP directions, suggesting similar creep properties everywhere within the small shale sample albeit they were different in the BN and BP directions.

The anisotropy of the shale sample is also evident in Figures 4 and 5. In the BN direction the maximum indentations at the end of the loading stage are generally larger than those in the BP direction, implying that the shale is more compliant in the BN direction. However, the variance of the moduli in the BN direction is higher. As mentioned earlier, the curves near the bottom of Figure 4 are considered as outliers and may have represented data points on locally hard minerals. Furthermore, data from Figures 4 and 5 reveal that the

viscosities in the BP direction are generally higher than in the BN direction, which resulted in creep occurring more slowly in the BP direction. All these results point to the shale sample being highly heterogeneous and strongly anisotropic.

3.3 Triaxial creep tests

Two cylindrical specimens were cored from the raw shale sample using a 1-inch coring bit at the Stanford Earth Materials Laboratory. One sample with a height of 28.5 mm was cored normal to the bedding plane, while the other with a height of 35.1 mm was cored parallel to the bedding plane. Both samples had a diameter of 23.7 mm.

The samples were tested with a loading system consisting of an MTS hydraulic loading frame and a high-pressure water cell at the John A. Blume Earthquake Engineering Center at Stanford University. The axial load was applied by the loading frame through a vertical shaft on top of the sample, and the axial displacement was measured with a linear variable differential transformer (LVDT) attached to the shaft. Since the applied load was much smaller than the capacity of the loading frame, an additional load cell was installed on the load frame to measure the axial load. The confining pressure inside the water cell was controlled and measured by a pressure transducer with a capacity of 14 MPa, which was connected to the water cell with steel pipes. To prevent water penetration, thin steel caps were glued to both ends of the sample with vacuum grease, and the sample was sealed inside a rubber membrane and constrained by two O-rings. After the tests, the membrane was removed and the samples were confirmed to be completely dry.

The water cell was filled at the beginning of the loading stage, and a small vertical load of around 0.1 kN was applied by the loading frame to ensure that the vertical shaft was in firm contact with the sample. Initially, the system was set to be displacement-controlled and no vertical displacement was allowed as the water pressure was gradually increased from zero to 10 MPa. The system was then switched to be force-controlled, and the axial load was raised to 13.8 kN over 90 s under a constant confining pressure to induce a differential stress of 19 MPa on the sample. This stress level, according to Sone and Zoback [72], was large enough for creep to be observed without causing damage to the samples. During the creep stage, the axial load was held constant and the deformation of the sample was recorded for another 12,000 s.

The stress-strain curves during the loading stage are plotted in Figure 6. No plastic yielding was observed from either curve, suggesting that the deformation was dominated by elastic compression. Comparing the two curves, we observe the anisotropy of shale at the triaxial test scale and see that the shale is stiffer in the BP direction. Based on the linear portion of the curves, the elastic moduli were estimated to be 4.6 GPa for loading along the BP direction and 3.5 GPa for loading along the BN direction. These values of elastic

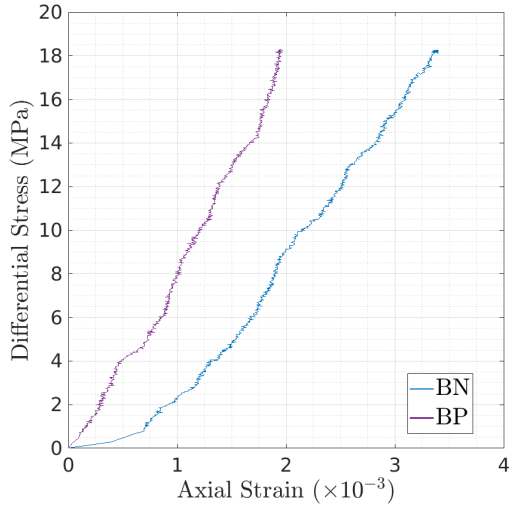

Fig. 6: Stress-strain responses of two samples during the triaxial compression loading stage.

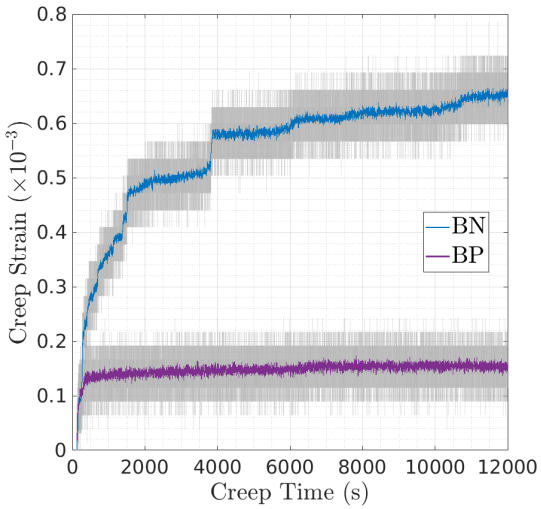

Fig. 7: Creep strains during the constant-load stage.

moduli were much smaller than the Young's moduli for Barnett, Haynesville or Eagle Ford shales as reported by Sone and Zoback [71].

Figure 7 shows the development of creep strains during the constant-load stage for the two samples. It should be mentioned that in a creep test the

axial load could only be controlled via a feedback loop on the displacement. Consequently, the axial load oscillated around the target value. The resulting raw creep responses also fluctuated significantly, and when connected with gray lines, the variations appeared as a gray area. For better visualization, the raw creep curves were smoothed using cubic splines into the blue and purple curves, from which the trends can be seen more clearly. The creep deformations are evident in the BN direction. The concave creep curve continues beyond 12,000 s, although the creep rate decreases with time. The total amount of creep strain reaches 6.5×10^{-4} at the end of the constant-load stage, which is about 10% of the total elastic strain that accumulated during the loading stage. However, the creep deformations in the BP direction are hardly noticeable, with the creep curve appearing nearly as a horizontal line. All these results confirm that the shale exhibited anisotropic creep behavior as well, with the creep deformation being greater in the BN direction than in the BP direction.

4 Analysis of test results

This section analyzes the results of nanoindentation and triaxial creep tests with the aim of unifying the two tests within the context of the Cam-Clay IX viscoplastic model. Because there is no closed-form solution available for indentation with a Berkovich indenter on a viscoplastic halfspace, the indentation process was simulated mechanistically with a FE model that employs the material model described in Section 2.2.

4.1 Simulation of indentation creep tests

The FE mesh consists of 8-node hexahedral elements and is shown in Figure 8. The diamond indenter is many times stiffer than the shale being indented, so we assumed it to be a rigid body with only one node defining its position in 3D space. The indentation process was simulated as a load-driven problem with the indenter load increasing with time up to a maximum value of 491 μN over a period of 30 seconds, after which it was held constant for 60 seconds to allow the shale to creep.

Except for the elastic moduli and viscosities, all material parameters were adopted from [11, 81] and are summarized in Table 2. These parameters define the yield surface and have been used to characterize yielding of Barnett and Woodford shales. As for the elastic moduli and viscosities, we assumed in this work that these two parameters were related in the sense that the higher the modulus, the higher the viscosity. More explicit relationships may be inferred from the nanoindentation curves of Figures 4 and 5. First, along each of the BN and BP directions we assumed a value of modulus and simulated the entire depth-time responses during the entire load-creep process. The viscosities were

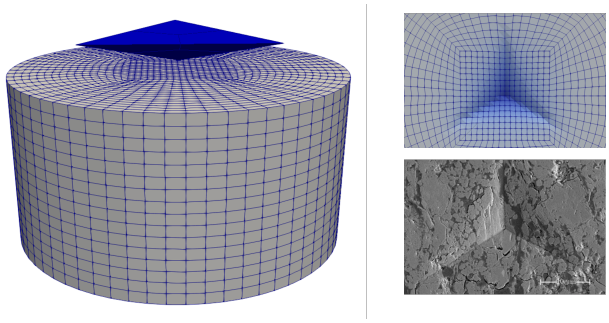

Fig. 8: FE mesh for indentation on a viscoplastic halfspace with a Berkovich-type nanoindenter (navy blue). The shale domain is a cylindrical solid with a diameter of 4 μm and a height of 2 μm; maximum indentation depth is 450 nm. Indent on the real shale reproduced from Bennett et al. [7].

Table 2: Plasticity parameters and initial yield stress for indentation simulations: c_1, c_2, c_3 = anisotropy parameters; M = slope of critical state line; λ^p = compressibility index; P_c = preconsolidation stress (tension is positive). See Semnani et al. [65].

Parameter	**Value**	**Unit**
c_1	0.6	-
c_2	-0.1	-
c_3	0.4	-
M	1.07	-
λ^p	-0.0003	-
P_c	-18	MPa

calibrated based on the slopes of the nanoindentation curves during the steady creep stage.

Five simulated response curves spanning the entire range of indentation-time responses are shown in Figure 9 for indentation in the BN direction, and in Figure 10 for indentation in the BP direction. For indentation in the BN direction, we did not consider the four indentation curves at the bottom of Figure 9 as they were considered as outliers in the earlier analysis. The moduli and viscosities inferred from the simulated results are plotted in Figure 11 and confirm the assumption that there is a relation between the two material parameters. The relationships obtained from linear regression take the form

$$\log \eta_\perp = 9.80 + 0.21 E_\perp \,, \qquad \log \eta_\parallel = 10.81 + 0.10 E_\parallel \,, \tag{6}$$

where η and E have the units as shown in Figure 11.

In principle, there should be as many simulation curves as there are experimental indentation-time curves to infer the correspoding modulus and viscosity at each indented point. However, for expediency, we simply performed a linear interpolation of the moduli values for the experimental indentation-

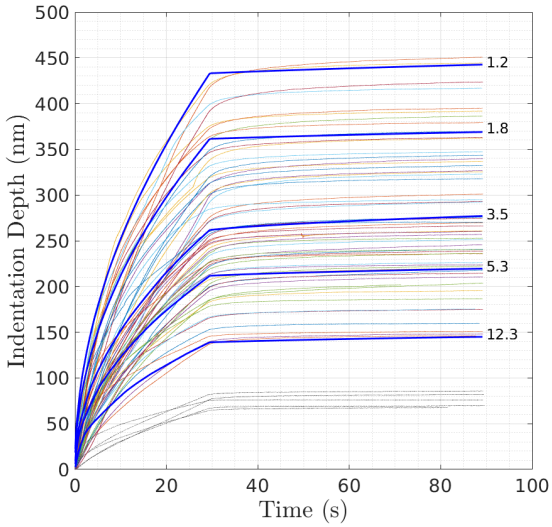

Fig. 9: Simulated indentation creep curves along the BN direction. Numbers next to the thick red lines are inferred elastic moduli in GPa.

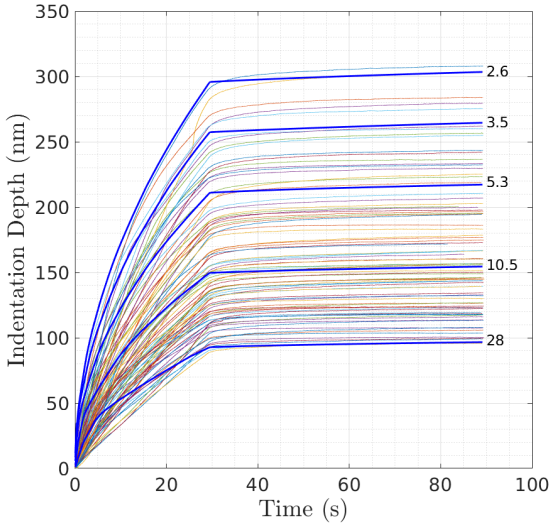

Fig. 10: Simulated indentation creep curves along the BP direction. Numbers next to the thick red lines are inferred elastic moduli in GPa.

time curves not intersected by the simulation response curves. The probability distributions of the moduli values for the shale sample were then inferred in

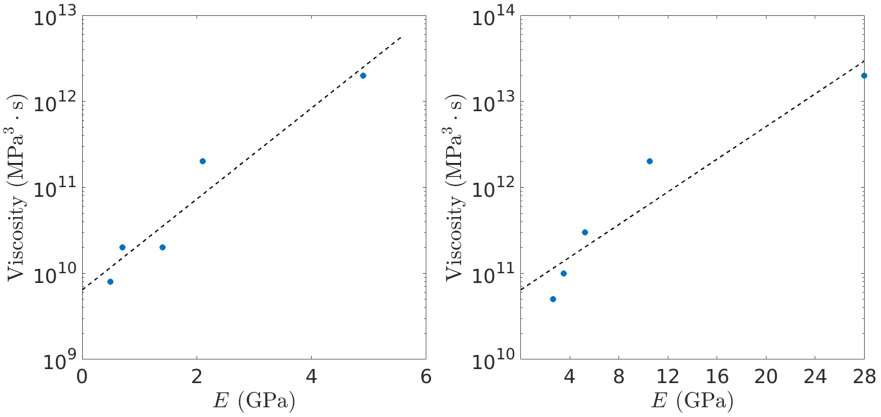

Fig. 11: Relation between calibrated viscosities and inferred moduli along the BN (left) and BP (right) directions.

Figure 12, which again affirms the inherent anisotropy of the shale as the measured responses are consistently stiffer in the BP direction than in the BN direction.

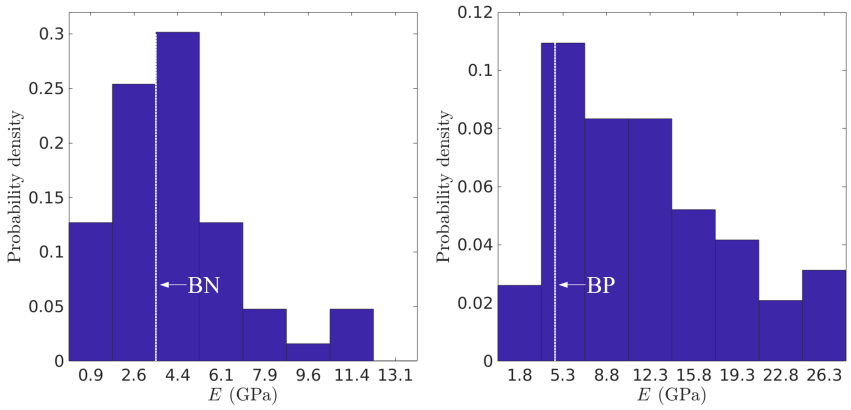

Fig. 12: Probability density functions for moduli in the BN (left) and BP (right) directions inferred from nanoindentation creep tests. Dotted white lines represent moduli values measured from triaxial creep tests.

Figure 12 also shows the normal probability distributions (represented by the red curves) that best fit the elastic moduli distributions. For the BN direction, the mean value of $E_\perp$ is 4.5 GPa, with a median of 3.9 GPa and standard deviation of 2.6 GPa. For the BP direction, the mean value of $E_\parallel$

is 12.1 GPa, with a median of 10.8 GPa and standard deviation of 6.8 GPa. In both directions the distributions are asymmetric and exhibit long tails resulting from the presence of locally stiff materials in the sample. Although Figures 4 and 5 suggest that the variation of the indentation depth is greater along the BN direction, after removing the outliers we find that the variance in moduli along the BN direction is actually smaller, which means that the shale sample is actually more heterogeneous with respect to inferred elastic moduli along the BP direction.

4.2 Simulation of triaxial creep tests

We have also simulated the triaxial creep tests on the same Woodford shale sample using the Cam-Clay IX viscoplastic model, but this time we used the creep parameters inferred from the nanoindentation creep tests presented in the previous section. The objective of the simulation was basically to answer the following question: *Can the material parameters obtained from nanoindentation creep tests be used to predict the results of triaxial creep tests?*

To answer this question, we constructed a cylindrical FE mesh with a diameter of 23.7 mm and a height of 28.5 mm shown in Figure 13, essentially replicating the dimensions of the triaxial shale sample cored normal to the bedding plane. The two samples (cored normal and parallel to bedding) were supported on smooth platens on both the top and bottom ends, so, without any imperfection they were expected to undergo homogeneous deformation. In that case, a stress-point simulation of the tests would theoretically be sufficient. Nevertheless, we still constructed the finite element mesh shown in Figure 13 to investigate the effects of spatial heterogeneity in the elastic modulus $E_\perp$. The simulation was stress-control, where the confining pressure was first increased from zero to 10 MPa over a period of 50 seconds, followed by an increase of differential stress from zero to 18.3 MPa over another 90 seconds. Thereafter, the sample was allowed to creep for 3 hours with all the loads held constant. For each of the BN and BP directions, the mean elastic modulus from the distributions shown in Figure 12 was used, and the corresponding viscosity was computed from Equation (6). All the remaining parameters were the same as those listed in Table 2. The simulated creep curves are plotted along with the experimental data in Figure 14.

Remarkably, Figure 14 shows that the anisotropic creep response of the shale sample in the BN direction was captured by our model quite accurately. The homogeneous and heterogeneous (in $E_\perp$) simulations generated nearly the same creep strain responses. We recall that the scales of the nanoindentation and triaxial creep tests are orders of magnitude apart on the metric scale, and that the nanoindentation creep tests lasted 60 seconds whereas the triaxial creep tests lasted more than 3 hours, yet the model predicted the triaxial creep response throughout the duration of the tests quite well. To get a better idea of the sensitivity of the model prediction to values of $E_\perp$, Figure 14 also plots the triaxial creep responses using the moduli values equal to the mean value ± 0.5

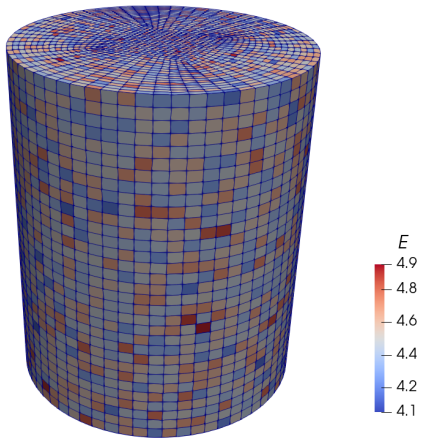

Fig. 13: Finite element mesh for triaxial creep simulations. Heterogeneity in $E_\perp$ was generated using a normal distribution with a mean of 4.5 GPa and a range as shown in the color bar (in GPa).

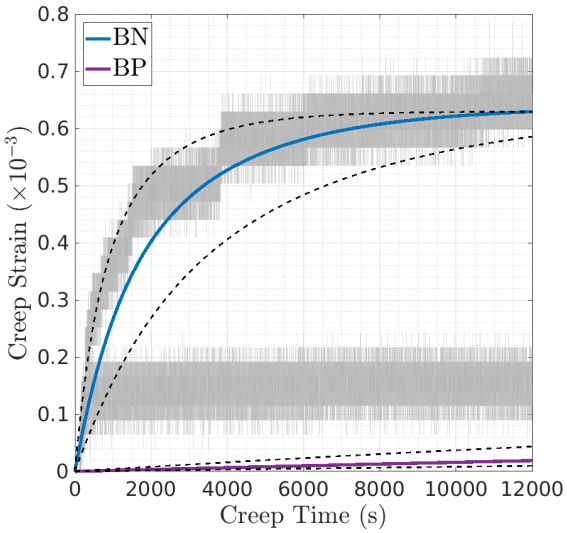

Fig. 14: Predicted triaxial creep curves plotted with the experimental data. Dashed curves are simulations at ±0.5 times standard deviation from the means of the elastic moduli $E_\perp$ and $E_\parallel$.

times the standard deviation. Although the band of the predicted responses is quite wide early on, the long-term creep strain (at 12,000 s) appears to be relatively insensitive to the values of the modulus. The viscosity calibrated

from the triaxial creep test was determined to be 4×10^{10} MPa$^3 \cdot$ s, which is slightly smaller than the indentation-viscosity of 5.5×10^{10} MPa$^3 \cdot$ s inferred from the mean modulus, but is still within $\pm 0.5\times$standard deviation.

On the other hand, for the BP direction the magnitude of the triaxial creep strain using data inferred from nanoindentation creep tests is much smaller than the experimentally observed creep strain. Such discrepancy could be due to the fact that the triaxial loading frame is displacement-controlled, i.e., the applied load may have continued to increase beyond the target value as the displacement was being adjusted to maintain a constant load. Nevertheless, both the experimentally observed and numerically predicted creep strains in BP direction are very small in comparison to the corresponding values in the BN direction, suggesting that most creep in this shale sample takes place in the BN direction.

Finally, we examine how the elastic moduli measured directly from triaxial tests are related to the moduli distributions developed from indentation tests. By plotting the experimentally measured elastic moduli from triaxial tests as vertical dotted lines in Figure 12, we find that these moduli values lie closer to the range of values of elastic moduli inferred from nanoindentation tests with the highest probability of occurrence (i.e., the tallest bar in the histogram). This leads us to conclude that the elastic moduli inferred from indentation tests, in both BN and BP directions, are closely related to the elastic moduli determined from triaxial tests.

5 Closure

Through the Cam-Clay IX viscoplastic model, we have shown that the creep responses of a shale at the nanometer scale may be correlated with the creep responses of a larger sample of the same shale at the millimeter scale. Experimental data from nanoindentation and triaxial creep tests on an organic-rich Woodford shale were used to bridge the two scales in space and time. We have shown that the two most important material parameters governing the creep behavior are the elastic moduli and viscosities of the rock. The shale sample was highly anisotropic—more precisely, transversely isotropic—so, to characterize the creep responses, the two pairs of material constants were determined for the same sample in both BN and BP directions.

We recognize that the strength of the correlation between the two scales of interest depends on the degree of heterogeneity of the rock sample. In fact, this has been demonstrated for the shale sample tested in this work: the sample was more homogeneous with respect to the elastic moduli in the BN direction than in the BP direction, and therefore, the moduli values exhibited a stronger correlation in the BN direction. Nevertheless, in spite of the large jumps in the spatiotemporal scales, from nanometers to millimeters and from seconds to hours, it is encouraging to see that the creep responses of a relatively

heterogeneous sample of shale correlated well in the weaker BN direction where the material exhibited greater creep deformation.

Acknowledgements

This work was supported by the U.S. National Science Foundation under Award Number CMMI-1914780.

Data availability statement

The datasets generated during the course of this study are available from the corresponding author upon reasonable request.

References

[1] Abedi S, Slim M, Hofmann R, Bryndzia T, Ulm FJ (2016). Nanochemo-mechanical signature of organic-rich shales: a coupled indentation–EDX analysis. Acta Geotechnica 11:559–572.

[2] Abel JF, Lee FT (1980). Subsidence potential in shale and crystalline rocks. Technical Report, US Geological Survey.

[3] Abousleiman Y, Tran M, Hoang S, Bobko C, Ortega A, Ulm, F-J (2007). Geomechanics field and laboratory characterization of Woodford shale: The next gas play. Society of Petroleum Engineers SPE 110120.

[4] Abousleiman Y, Cheng A H-D, Jiang C, Roegiers J-C (1996). Poroviscoelastic analysis of borehole and cylinder problems. Acta Mechanica 119:119–219.

[5] Akono A-T, Chen J, Zhan M, Shah SP (2021). Basic creep and fracture response of fine recycled aggregate concrete. Construction and Building Materials 266A:121107.

[6] Almasoodi MM, Abousleiman Y, Hoang SK (2014). Viscoelastic creep of Eagle Ford Shale: Investigating fluid-shale interaction. SPE/CSUR Unconventional Resources Conference–Canada. Society of Petroleum Engineers SPE-171569-MS.

[7] Bennett KC, Berla LA, Nix WD, Borja RI (2015). Instrumented nanoindentation and 3D mechanistic modeling of a shale at multiple scales. Acta Geotechnica 10(1):1–14.

[8] Bernabe Y, Fryer DT, Shively RM (1994). Experimental observations of the elastic and inelastic behaviour of porous sandstones. Geophysical Journal International 117(2):403–418.

[9] Bobko CP (2008). Assessing the mechanical microstructure of shale by nanoindentation: The link between mineral composition and mechanical properties. PhD thesis, Massachusetts Institute of Technology, Cambridge, Massachusetts.

[10] Boggs Jr S (2009). Petrology of sedimentary rocks. Cambridge University Press.
[11] Borja RI, Yin Q, Zhao Y (2020). Cam-Clay plasticity. Part IX: On the anisotropy, heterogeneity, and viscoplasticity of shale. Computer Methods in Applied Mechanics and Engineering 360:112695.
[12] Borja RI (2016). On the mechanical energy and effective stress in saturated and unsaturated porous continua. International Journal of Solids and Structures 43(6):1764–1786.
[13] Borja RI, Choo J (2016). Cam-Clay plasticity. Part VIII: A constitutive framework for porous materials with evolving internal structure. Computer Methods in Applied Mechanics and Engineering 309:653–679.
[14] Borja RI (2013). Plasticity Modeling & Computation, Springer, Berlin-Heidelberg.
[15] Borja RI (1985). A constitutive model for the stress-strain-time behaviour of 'wet' clays. Géotechnique 35(3):283–298.
[16] Brantut N, Baud P, Heap MJ, Meredith PG (2012). Micromechanics of brittle creep in rocks. Journal of Geophysical Research: Solid Earth 117(B8).
[17] Brantut N, Heap MJ, Meredith PG, Baud P (2013). Time-dependent cracking and brittle creep in crustal rocks: A review. Journal of Structural Geology 52:17–43.
[18] Celleri HM, Sanchez M (2021). Hydraulic fracture propagation barriers induced by weak interfaces in anisotropic rocks. International Journal for Numerical and Analytical Methods in Geomechanics 45(14): 2155–2173.
[19] Chang C, Zoback MD (2008). Creep in unconsolidated shale and its implication on rock physical properties. In The 42nd US Rock Mechanics Symposium (USRMS). American Rock Mechanics Association.
[20] Chang C, Zoback MD. (2010). Viscous creep in room-dried unconsolidated Gulf of Mexico shale (II): Development of a viscoplasticity model. Journal of Petroleum Science and Engineering 72:50–55.
[21] Chester FM, Chester JS, Kronenberg AK, Hajash A (2007). Subcritical creep compaction of quartz sand at diagenetic conditions: Effects of water and grain size. Journal of Geophysical Research: Solid Earth 112(B6).
[22] Choo J, Semnani SJ, White JA (2021). An anisotropic viscoplasticity model for shale based on layered microstructure homogenization. International Journal for Numerical and Analytical Methods in Geomechanics 45(4):502–520.
[23] Choo J, White JA, Borja RI (2018). Hydromechanical modeling of unsaturated flow in double porosity media. International Journal of Geomechanics 16(6):D4016002.
[24] Delage P, Belmokhtar M (2022). Drained triaxial testing of shales: insight from the Opalinus Clay. Acta Geotechnica 17(7): 2855–2874.
[25] Den Brok SWJ, Spiers CJ (1991). Experimental evidence for water weakening of quartzite by microcracking plus solution–precipitation creep. Journal of the Geological Society 148(3):541–548.

[26] De Waal JA, Smits RMM (1988). Prediction of reservoir compaction and surface subsidence: Field application of a new model. SPE Formation Evaluation 3(2):347–356.

[27] Du J, Luo S, Hu L, Guo B, Guo D, Zhang G (2022). Multiscale mechanical properties of shales: grid nanoindentation and statistical analytics. Acta Geotechnica 17(2): 339–354.

[28] Duvaut G, Lions JL (1976). Inequalities in Mechanics and Physics, Springer-Verlag, Berlin-Heidelberg.

[29] Gathier B (2008). Multiscale strength homogenization: Application to shale nanoindentation. PhD thesis, Massachusetts Institute of Technology, Cambridge, Massachusetts.

[30] Gupta N, Mishra B (2021). Influence of stress-induced microcracks on viscoplastic creep deformation in Marcellus shale. Acta Geotechnica 16(5): 1575–1595.

[31] Hartley RR, Behringer RP (2003). Logarithmic rate dependence of force networks in sheared granular materials. Nature 421(6926):928–931.

[32] Hoang SK, Abousleiman YN (2009). Poroviscoelastic two-dimensional anisotropic solution with application to articular cartilage testing. Journal of engineering mechanics 135(5): 367–374.

[33] Hoang SK, Abousleiman YN (2012). Correspondence principle between anisotropic poroviscoelasticity and poroelasticity using micromechanics and application to compression of orthotropic rectangular strips. Journal of Applied Physics 112(4): 044907.

[34] Horsrud P, Holt RM, Sonstebo EF, Svano G, Bostrom B (1994). Time dependent borehole stability: laboratory studies and numerical simulation of different mechanisms in shale. In Rock Mechanics in Petroleum Engineering. Society of Petroleum Engineers.

[35] Ip SCY, Choo J, Borja RI (2021). Impacts of saturation-dependent anisotropy on the shrinkage behavior of clay rocks. Acta Geotechnica 16:3381–3400.

[36] Ip SCY, Borja RI (2022). Evolution of anisotropy with saturation and its implications for the elastoplastic responses of clay rocks. International Journal for Numerical and Analytical Methods in Geomechanics 46:23–46.

[37] Ip SC, Borja RI (2023). Multiscale interactions of elastic anisotropy in unsaturated clayey rocks using a homogenization model. Acta Geotechnica 18:2289–2307.

[38] Kabir P, Ulm FJ, Akono AT (2017). Rate-independent fracture toughness of gray and black kerogen-rich shales. Acta Geotechnica 12:1207–1227.

[39] Kabwe E, Karakus M, Chanda EK (2020). Creep constitutive model considering the overstress theory with an associative viscoplastic flow rule. Computers and Geotechnics 124:103629.

[40] Kamali-Asl A, Ghazanfari E (2017). Investigating the creep response of Marcellus shale formations. In Geotechnical Frontiers 2017:562–569.

[41] Kemeny JM (1991). A model for non-linear rock deformation under compression due to sub-critical crack growth. In International journal of rock mechanics and mining sciences geomechanics abstracts 28(6):459–467.

[42] Kumar V, Curtis ME, Gupta N, Sondergeld CH, Rai CS (2012). Estimation of elastic properties of organic matter in Woodford shale nanoindentation measurements. SPE Canadian Unconventional Resources Conference. Society of Petroleum Engineers, SPE-162778-MS.

[43] Kumar V, Sondergeld CH, Rai CS (2012). Nano to macro mechanical characterization of shale. SPE Annual Technical Conference and Exhibition. Society of Petroleum Engineers, SPE-159804-MS.

[44] Kwok CY, Duan K, Pierce M (2020). Modeling hydraulic fracturing in jointed shale formation with the use of fully coupled discrete element method. Acta Geotechnica 15: 245–264.

[45] Li Y, Ghassemi A (2012). Creep behavior of Barnett, Haynesville, and Marcellus shale. 46th US Rock Mechanics/Geomechanics Symposium, American Rock Mechanics Association ARMA-2012-330.

[46] Liu K, Ostadhassan M, Bubach B (2016). Applications of nanoindentation methods to estimate nanoscale mechanical properties of shale reservoir rocks. Journal of Natural Gas Science and Engineering 35:1310–1319.

[47] Liu K, Ostadhassan M, Bubach B (2018). Application of nanoindentation to characterize creep behavior of oil shales. Journal of Petroleum Science and Engineering 167:729–736.

[48] Liu K, Rassouli F., Liu B, Ostadhassan M (2020). Creep Behavior of Shale: Nanoindentation vs. Triaxial Creep Tests. Rock Mechanics and Rock Engineering 1–15.

[49] Liu Y, Borja RI (2022). Time scales in the primary and secondary compression of soils. International Journal for Numerical and Analytical Methods in Geomechanics 46(8): 1383–1408.

[50] Lomnitz C (1956). Creep measurements in igneous rocks. The Journal of Geology 64(5):473–479.

[51] Lyu C, Xu D, Liu J, Ren Y, Liang C, Zhao C (2023). Investigation on very long-term brittle creep test and creep-damage constitutive model for granite. Acta Geotechnica, https://doi.org/10.1007/s11440-022-01790-4.

[52] Ma S, Gutierrez M (2021). Determination of the poroelasticity of shale. Acta Geotechnica 16: 581–594.

[53] Mehana M, Santos JE, Neil C, Carey JW, Guthrie G, Hyman J, Kang Q, Karra S, Sweeney M, Xu H, Viswanathan H (2022). Shale fundamentals: Experimental and modeling insights. Energy Reports 8:11192–11205.

[54] Menefee AH, Welch, NJ, Frash LP, Hicks W, Carey JW, Ellis BR (2020). Rapid mineral precipitation during shear fracturing of carbonate-rich shales. Journal of Geophysical Research: Solid Earth 125(6), e2019JB018864.

[55] Mighani S, BernabE Y, Boulenouar A, Mok U, Evans B (2019). Creep deformation in Vaca Muerta shale from nanoindentation to triaxial experiments. Journal of Geophysical Research: Solid Earth 124(8):7842–7868.
[56] Mishra B, Verma P (2015). Uniaxial and triaxial single and multistage creep tests on coal-measure shale rocks. International Journal of Coal Geology 137:55–65.
[57] McLamore R, Gray KE (1967). The mechanical behavior of anisotropic sedimentary rocks. Journal of Engineering for Industry 89(1):62–73.
[58] Nguyen-Sy T, Vu MN, Nguyen TT (2021). A hybrid Laplace-Galerkin method for thermo-hydro-mechanical coupling in fluid saturated porous media: Application for borehole problems. International Journal for Numerical and Analytical Methods in Geomechanics 45(14): 2102–2112.
[59] Niandou H, Shao J, Henry J, Fourmaintraux D (1997). Laboratory investigation of the mechanical behaviour of Tournemire shale. International Journal of Rock Mechanics and Mining Sciences 34(1):3–16.
[60] Perzyna P (1966). Fundamental problems in viscoplasticity. Advances in Applied Mechanics 9:244–368.
[61] Pettijohn FJ (1975). Sedimentary rocks, 3rd Edition. Harper & Row Publishers, New York.
[62] Rassouli FS, Zoback MD (2015). Long-term creep experiments on Haynesville shale rocks. 49th US Rock Mechanics/Geomechanics Symposium, American Rock Mechanics Association ARMA-2015-532.
[63] Rassouli FS, Zoback MD (2018). Comparison of short-term and long-term creep experiments in shales and carbonates from unconventional gas reservoirs. Rock Mechanics and Rock Engineering 51(7):1995–2014.
[64] Rybacki E, Herrmann J, Wirth R, Dresen G (2017). Creep of Posidonia shale at elevated pressure and temperature. Rock Mechanics and Rock Engineering 50: 3121–3140.
[65] Semnani SJ, White JA, Borja RI (2016). Thermo-plasticity and strain localization in transversely isotropic materials based on anisotropic critical state plasticity. International Journal for Numerical and Analytical Methods in Geomechanics 40:2423–2449.
[66] Semnani SJ, Borja RI (2017). Quantifying the heterogeneity of shale through statistical combination of imaging across scales. Acta Geotechnica 12:1193–1205.
[67] Semnani SJ, White JA (2020). An inelastic homogenization framework for layered materials with planes of weakness. Computer Methods in Applied Mechanics and Engineering 370:113221.
[68] Shi HL, Hosdez J, Rougelot T, Xie SY, Shao JF, Talandier J (2021). Influences of structural anisotropy and heterogeneity on three-dimensional strain fields and cracking patterns of a clay-rich rock. Acta Geotechnica 16: 2175–2187.
[69] Shukla P, Kumar V, Curtis M, Sondergeld CH, Rai CS (2013). Nanoindentation studies on shales. In 47th US Rock Mechanics/Geomechanics Symposium. American Rock Mechanics Association.

[70] Simo JC, Hughes TJR (1998). Computational Inelasticity, Springer, Berlin-Heidelberg.
[71] Sone H, Zoback MD (2013). Mechanical properties of shale-gas reservoir rocks — Part 1: Static and dynamic elastic properties and anisotropy. Geophysics 78(5): D381–D392.
[72] Sone H, Zoback MD (2013). Mechanical properties of shale-gas reservoir rocks — Part 2: Ductile creep, brittle strength, and their relation to the elastic modulus. Geophysics 78(5):D393–D402.
[73] Sone H, Zoback MD (2014). Time-dependent deformation of shale gas reservoir rocks and its long-term effect on the in situ state of stress. International Journal of Rock Mechanics and Mining Sciences 69:120–132.
[74] Tian H, Xu T, Wang F, Patil VV, Sun Y, Yue G (2014). A numerical study of mineral alteration and self-sealing efficiency of a caprock for CO_2 geological storage. Acta Geotechnica 9:87–100.
[75] Tougaard S, Jørgensen B (1984). Inelastic background intensities in XPS spectra. Surface Science 143(2–3): 482–494.
[76] Tounsi H, Rutqvist J, Hu M, Wolters R, Lerche S (2023). Long-term sinking of nuclear waste canisters in salt formations by low-stress creep at high temperature. Acta Geotechnica: 1–16.
[77] Ulm F-J, Vandamme M, Bobko C, Alberto-Ortega J, Tai K, Ortiz C (2007). Statistical indentation techniques for hydrated nanocomposites: Concrete, bone, and shale. Journal of the American Ceramic Society 90(9):2677–2692.
[78] Ulm F-J, Abousleiman Y (2006). The nanogranular nature of shale. Acta Geotechnica 1:77–88.
[79] Vandamme M, Ulm FJ (2009). Nanogranular origin of concrete creep. Proceedings of the National Academy of Sciences 106(26): 10552–10557.
[80] Wilkinson DS, Ashby MF (1975). Pressure sintering by power law creep. Acta Metallurgica 23(11):1277–1285.
[81] Yin Q, Liu Y, Borja RI (2021). Mechanisms of creep in shale from nanoscale to specimen scale. Computers and Geotechnics 136:104138.
[82] Xie H, Li X, Fang Z, Wang Y, Li Q, Shi L, Bai B, Wei N, Hou Z (2014). Carbon geological utilization and storage in China: current status and perspectives. Acta Geotechnica 9:7–27.
[83] Xu B, Yuan Y, Wang Z (2011). Thermal impact on shale deformation/failure behaviors—Laboratory studies. 45th US Rock Mechanics/Geomechanics Symposium. American Rock Mechanics Association ARMA-11-303.
[84] Zhang L, Zhou H, Wang X, Wang L, Su T, Wei Q, Deng T (2021). A triaxial creep model for deep coal considering temperature effect based on fractional derivative. Acta Geotechnica: 1–13.
[85] Zhao Y, Semnani SJ, Yin Q, Borja RI (2018). On the strength of transversely isotropic rocks. International Journal for Numerical and Analytical Methods in Geomechanics 42:1917–1934.

[86] Zhang Q, Borja RI (2021). Poroelastic coefficients for anisotropic single and double porosity media. Acta Geotechnica 16:3013–3025.

[87] Zhao Y, Borja RI (2020). A continuum framework for coupled solid deformation–fluid flow through anisotropic elastoplastic porous media. Computer Methods in Applied Mechanics and Engineering 369:113225.

[88] Zhao Y, Borja RI (2021). Anisotropic elastoplastic response of double-porosity media. Computer Methods in Applied Mechanics and Engineering 380:113797.

[89] Zhao Y, Borja RI (2022). A double-yield-surface plasticity theory for transversely isotropic rocks. Acta Geotechnica 17(11):5201–5221.